Accumulation and Subduction of Buoyant Material at Submesoscale Fronts

JOHN R. TAYLOR

Department of Applied Mathematics and Theoretical Physics, University of Cambridge, Cambridge, United Kingdom

(Manuscript received 22 December 2017, in final form 11 April 2018)

ABSTRACT

The influence of submesoscale currents on the distribution and subduction of passive, buoyant tracers in the mixed layer is examined using large-eddy simulations. Submesoscale eddies are generated through an ageostrophic baroclinic instability associated with a background horizontal buoyancy gradient. The simulations also include various levels of surface cooling, which provides an additional source of three-dimensional turbulence. Submesoscales compete against turbulent convection and restratify the mixed layer while generating strong turbulence along a submesoscale front. Buoyant tracers accumulate at the surface along the submesoscale front where they are subducted down into the water column. The presence of submesoscales strongly modifies the vertical tracer flux, even in the presence of strong convective forcing. The correlation between high tracer concentration and strong downwelling enhances the vertical diffusivity for buoyant tracers.

1. Introduction

A wide range of buoyant material can be found near the ocean surface. Here, buoyant material is defined as particles or droplets that move upward relative to the surrounding water because of their buoyancy. This definition includes bubbles, some types of phytoplankton, oil droplets, and microplastics. Buoyant material plays an important role in air–sea gas exchange, biogeochemical cycles, fisheries, and pollutant transport.

Buoyant material is generally not uniformly distributed across the ocean surface but instead accumulates in regions of surface convergence where it can be pulled below the surface by strong downwelling currents. For example, Langmuir circulations are known to cause oil, bubbles, and microplastics to accumulate in narrow rows with enhanced surface convergence and downwelling (Thorpe 2000; Kukulka and Brunner 2015; Brunner et al. 2015). Downwelling of high concentrations of buoyant material enhances the vertical flux (Veron and Melville 2001) and can significantly modify the equilibrium vertical distribution of the buoyant material (Kukulka and Brunner 2015).

Here, turbulence-capturing large-eddy simulations (LES) are used to study the influence of submesoscales on the accumulation and subduction of buoyant material. Submesoscales are dynamical features characterized by horizontal scales from 0.1 to 10 km and a Rossby number $\mathrm{Ro} \equiv U/(fL) \sim 1$, where U and L are characteristic horizontal velocity and length scales and f is the Coriolis parameter. Submesoscales have been implicated in increasing the stratification of the upper ocean (Fox-Kemper et al. 2008; Mahadevan et al. 2012; Bachman and Taylor 2016; Callies and Ferrari 2018) and enhancing vertical tracer fluxes (Thomas et al. 2008; Omand et al. 2015) while reducing the rate of turbulent mixing (Taylor and Ferrari 2011; Taylor 2016).

Submesoscales are often generated through a variety of ageostrophic instabilities associated with large-scale currents. These instabilities include mixed layer baroclinic instability (MLI) and symmetric instability (SI), which generate submesoscale flows at the expense of potential energy (as for MLI) and kinetic energy (as for SI) associated with broader density fronts in thermal wind balance. This represents a downscale transfer of energy as has been confirmed by numerical simulations (Capet et al. 2008).

The shear and horizontal convergence associated with submesoscale currents can enhance existing horizontal density gradients through a process known as frontogenesis. This results in "submesoscale fronts," elongated regions with an abrupt change in density with an alongfront length of 0.1–10km. While frontogenesis also

Corresponding author: John R. Taylor, j.r.taylor@damtp.cam.ac.uk

Publisher's Note: This article was revised on 19 December 2018 to include a data availability statement in the Acknowledgments section that was missing when originally published.

DOI: 10.1175/JPO-D-17-0269.1

occurs on larger scales, the relatively large Rossby number associated with submesoscale flows can lead to rapidly intensifying submesoscale fronts and gravity wave generation (Shakespeare and Taylor 2014, 2015, 2016). Here, we will show that submesoscale fronts can be associated with strong surface convergence and downwelling, which results in accumulation and subduction of buoyant material.

Here, in addition to the downscale transfer of energy from the submesoscale, small-scale turbulence is generated by imposing a constant destabilizing surface heat flux that is varied between four simulations. The simulations presented here do not include the effects of wind or waves. The simulations do not attempt to replicate mixed layer turbulence under a certain set of realistic conditions but instead examine the influence of submesoscales and convection on buoyant material under controlled conditions. In addition, several classes of buoyant material are modeled, each using a constant slip velocity (equivalent to a constant particle or droplet size). Interactions between the size classes are neglected. The primary objective of this study is to examine the influence of submesoscales and convection on the distribution of buoyant tracers in a controlled environment with the hope that the results will motivate and guide future work under more realistic conditions.

2. Simulation setup

The configuration of the simulations is very similar to the setup used in Taylor (2016). Specifically, the computational domain is 1 km in each horizontal direction and 140 m in the vertical. The LES model solves the low-pass-filtered nonhydrostatic Boussinesq Navier–Stokes equations. The resolved fields are discretized on a grid with 512 points in each horizontal direction and 65 points in the vertical with a constant grid spacing of 1.95 m in the horizontal directions and variable grid spacing ranging from 1.25 to 2.87 m in the vertical direction. No stress boundary conditions are applied to the horizontal velocity at the top and bottom of the domain where the vertical velocity is set to zero. Further details of the numerical method are available in Taylor (2016, 2008).

A linear equation of state is used, and potential density (or buoyancy) is treated using a single scalar variable in the model. A relatively weak background density gradient is included using the "frontal zone" configuration used in previous studies (Thomas 2005; Taylor and Ferrari 2010; Taylor 2016). Specifically, the buoyancy is decomposed according to $b_T(x, y, z, t) = b(x, y, z, t) + M^2 x$, where b_T is the total buoyancy and M^2 is a constant background buoyancy gradient. Periodic boundary conditions are then applied to b in both horizontal directions. This has the effect of keeping the buoyancy difference across the domain constant. The LES model then solves the following equation for b:

$$\frac{\partial b}{\partial t} + \mathbf{u} \cdot \nabla b + uM^2 = \nabla \cdot [(\kappa + \kappa_{\mathrm{SGS}})\nabla b], \qquad (1)$$

where $\mathbf{u}$ is the resolved velocity, $u = \mathbf{u} \cdot \hat{\mathbf{x}}$, and κ is a small "molecular" diffusivity and $\kappa_{\mathrm{SGS}}(x, y, z, t)$ is the subgrid-scale diffusivity. For simplicity the subgrid-scale Prandtl number is set to unity such that $\kappa_{\mathrm{SGS}} = \nu_{\mathrm{SGS}}$, where ν_{SGS} is the subgrid-scale viscosity. A small constant diffusivity, $\kappa = 10^{-6}\,\mathrm{m^2\,s^{-1}}$, is used to ensure numerical stability, although this is much smaller than κ_{SGS}. The subgrid-scale model is the same as used in Taylor and Ferrari (2010).

The initial buoyancy profile is set using a very weak stratification in the upper 60 m with a buoyancy gradient $b_z = N^2 = 9 \times 10^{-8}\,\mathrm{s^{-2}}$ overlying a more stratified layer with $N^2 = 1.8 \times 10^{-6}\,\mathrm{s^{-2}}$. The background buoyancy gradient is held fixed at $M^2 = 3 \times 10^{-8}\,\mathrm{s^{-2}}$ such that the total buoyancy at $t = 0$ is

$$b_T(x, y, z, t = 0) = \int_0^z N^2(z')\,dz' + M^2 x. \qquad (2)$$

The Coriolis parameter is $f = 10^{-4}\,\mathrm{s^{-1}}$. As a result, the initial balanced Richardson number $\mathrm{Ri}_B = N^2 f^2 / M^4 = 1$ and 20 in the upper and lower layers, respectively. The velocity is initialized in thermal wind balance with the addition of random white noise with amplitude $10^{-6}\,\mathrm{m\,s^{-1}}$. The simulation parameters are chosen such that the flow is stable with respect to SI and the most unstable mode of mixed layer BCI has a wavelength approximately equal to the horizontal domain size $\simeq$1 km (Stone 1966; Fox-Kemper et al. 2008). The smallest unstable mode in the lower layer has a wavelength larger than 4 km (Stone 1966) and will therefore not be captured in the simulations.

The simulations are forced by applying a constant surface buoyancy flux B_0 equivalent to cooling the ocean surface. The magnitude of the surface buoyancy flux is varied in four simulations, from $B_0 = 0$ (unforced) to $B_0 = -1.9 \times 10^{-8}\,\mathrm{m^2\,s^{-3}}$. As described in Taylor (2016), the surface buoyancy flux competes with submesoscales to set the mixed layer stratification. The ratio of the surface buoyancy flux to the restratifying submesoscale buoyancy flux associated with using the parameterization of Fox-Kemper et al. (2008) takes the form

$$R_{\mathrm{MLI}} = \frac{B_0 f}{M^4 H^2}, \qquad (3)$$

and here, R_{MLI} ranges from 0 to 0.6 (see Table 1). Note that while this definition is consistent with Taylor (2016)

TABLE 1. Simulation parameters.

L_x, L_y, L_z (m)	Δx, Δy, Δz (m)	M^2 (s^{-2})	f (s^{-1})	$B_0 \times 10^8$ ($m^2 s^{-3}$)	R_{MLI}
1000, 1000, 140	2, 2, 1.3–3	3×10^{-8}	10^{-4}	(0, −0.019, −0.19, −1.9)	(0, 0.006, 0.06, 0.6)
250, 250, 140	2, 2, 1.3–3	0	10^{-4}	(0, −0.019, −0.19, −1.9)	—

and Callies and Ferrari (2018), when this ratio was defined in Mahadevan et al. (2010, 2012), a coefficient $C_e = 0.06$ was included in the denominator, and hence the values of R_{MLI} are equivalent to $S = 0, 0.1, 1, 10$ in the notation of Mahadevan et al. (2012). Mahadevan et al. (2012) hypothesized that when $S < 1$, restratification induced by submesoscale eddies would overcome convectively driven mixing. Hence, the chosen values of $R_{MLI} = 0.006$, 0.06, and 0.6 correspond to weak, moderate, and strong convection relative to the anticipated restratification. Note, however, that Taylor (2016) and Callies and Ferrari (2018) found persistent (albeit weak) stratification for $R_{MLI} \geq 0.6$.

To identify the influence of the horizontal buoyancy gradient and submesoscale dynamics, another set of simulations is run without a background buoyancy gradient; that is, $M^2 = 0$ in Eq. (1). Since these simulations do not start with available potential energy or thermal wind shear, and since the surface cooling is homogeneous, submesoscales do not develop. Instead, when surface cooling is applied, a statistically homogeneous convective layer develops. Since the horizontal scales associated with convection are relatively small, a smaller domain size of 250 m is used in each horizontal direction, while the grid spacing is the same as in the first set of simulations. The parameters in both sets of simulations are listed in Table 1.

Here, we use the same approach as in Kukulka and Brunner (2015) and model buoyant material as a continuous concentration of individual noninteracting particles. Each particle is assumed to move with the local fluid velocity plus an additional constant upward "slip" velocity. This is equivalent to assuming an instantaneous balance between the buoyant force and friction on the rising particle and is valid for small Stokes number and constant particle size. The equation for the concentration of buoyant material, or buoyant tracers, is

$$\frac{\partial c}{\partial t} + \mathbf{u} \cdot \nabla c + w_s \frac{\partial c}{\partial z} = \nabla \cdot [(\kappa + \kappa_{SGS}) \nabla c], \qquad (4)$$

where w_s is a constant slip velocity and κ and κ_{SGS} are the same as introduced above in the buoyancy equation. Four tracers will be considered, with different slip velocities, $w_s = (0, 0.05, 0.5, 5)$ mm s^{-1}. The numerical method used to solve the buoyant tracer equations is the same as described above for momentum and buoyancy, except that the term involving advection by the slip

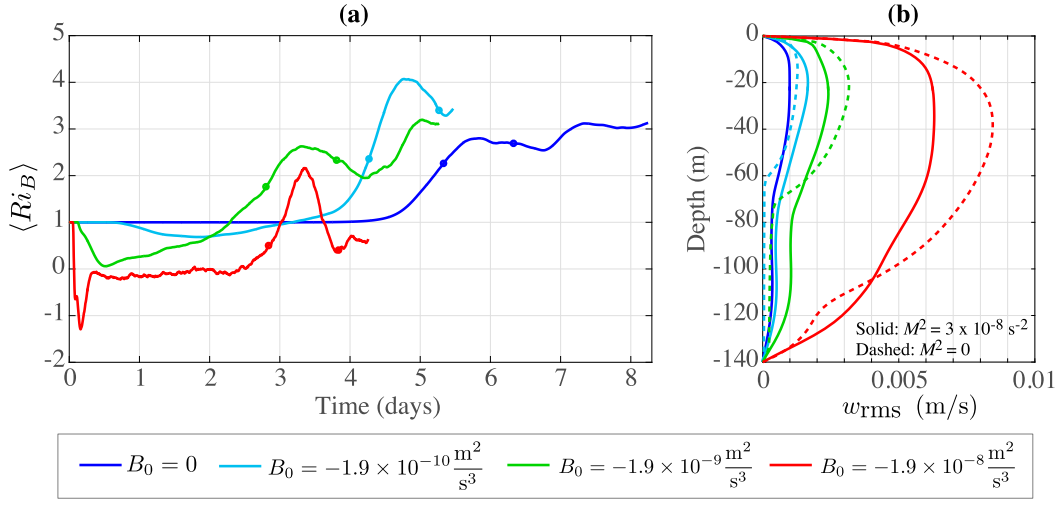

FIG. 1. (a) Balanced Richardson number, $\langle \mathrm{Ri}_B \rangle = \langle N^2 \rangle f^2 / M^4$, where angle brackets denote an average over both horizontal directions and from $-40 < z < -20$ m. Dots indicate the start and end of the window used for time averaging. (b) Vertical profiles of the rms vertical velocity, averaged over the time interval shown in (a).

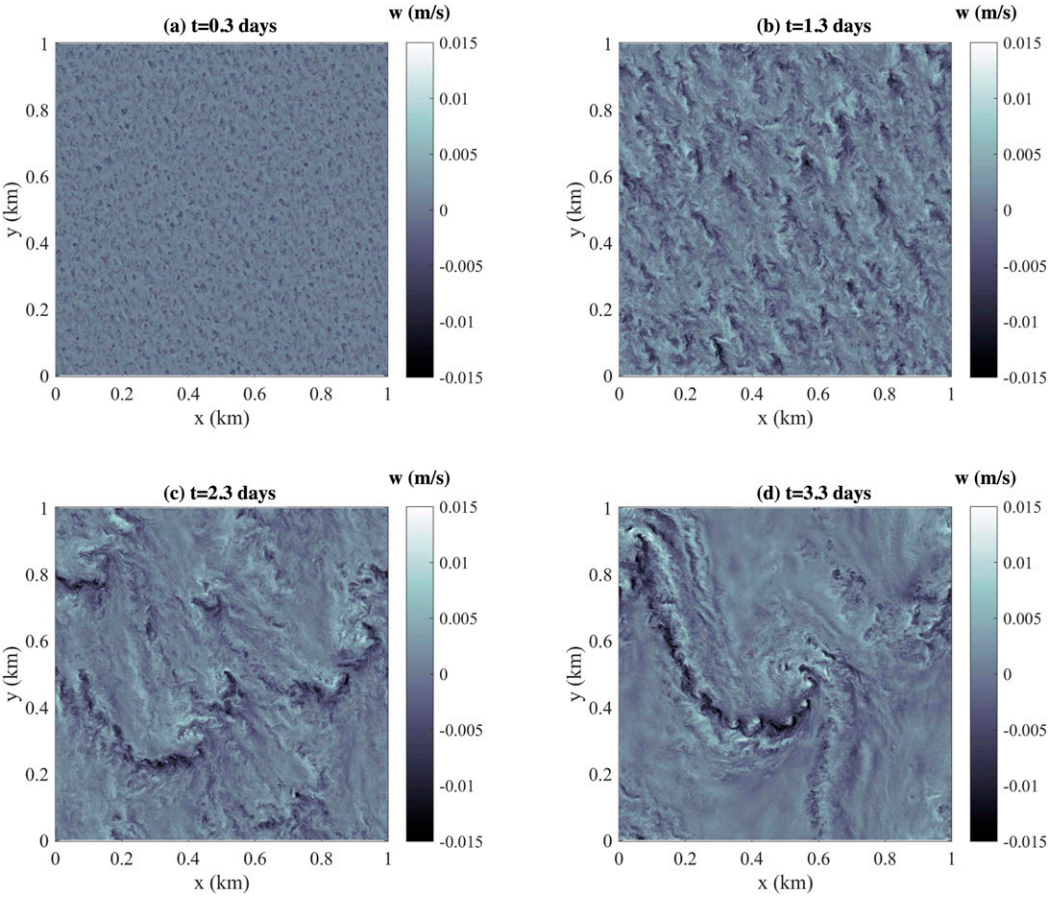

FIG. 2. Horizontal cross sections of the vertical velocity from the simulation with $M^2 = 3 \times 10^{-8}\,\mathrm{s}^{-2}$ and $B_0 = -1.9 \times 10^{-9}\,\mathrm{m^2\,s^{-3}}$ at $z = -25\,\mathrm{m}$.

velocity is treated with an upwinding scheme for numerical stability. The initial conditions for all tracers is $c(t = 0) = e^{z/d}$, where $d = 10\,\mathrm{m}$, independent of both horizontal directions and normalized such that $c(z = 0, t = 0) = 1$.

One minor difference between the simulations here and those in Taylor (2016) is the spinup. In Taylor (2016), MLI was allowed to develop until the submesoscale flow reached a finite amplitude before the surface cooling was started and the phytoplankton concentration was initialized. This ensured that the time needed for submesoscales to develop was the same regardless of the strength of surface cooling—an important feature for comparing the biological response in each simulation since the phytoplankton concentration grew or decayed exponentially in time. Here, since the tracer concentration is conserved, this spinup period is not needed, and velocity, buoyancy, and buoyant tracers are initialized at the same time ($t = 0$) and the surface heat flux is constant throughout the simulation. As a result, MLI develops in a mixed layer with active turbulent convection in the forced simulations with $B_0 \neq 0$.

3. Results

a. Flow description

Figure 1a shows a time series of the stratification, averaged in the central portion of the mixed layer, $-40 < z < -20\,\mathrm{m}$, and over the full horizontal domain. MLI develops more rapidly in the simulations with moderate and strong convection compared to the unforced case. Somewhat paradoxically, this causes mixed layer stratification to develop sooner in the simulations with convection. Once stratification develops, its strength and vertical structure are very similar to those reported in Taylor (2016). All time averages reported below will be calculated using a time window of one day centered at the time of maximum mixed layer stratification. While somewhat arbitrary,

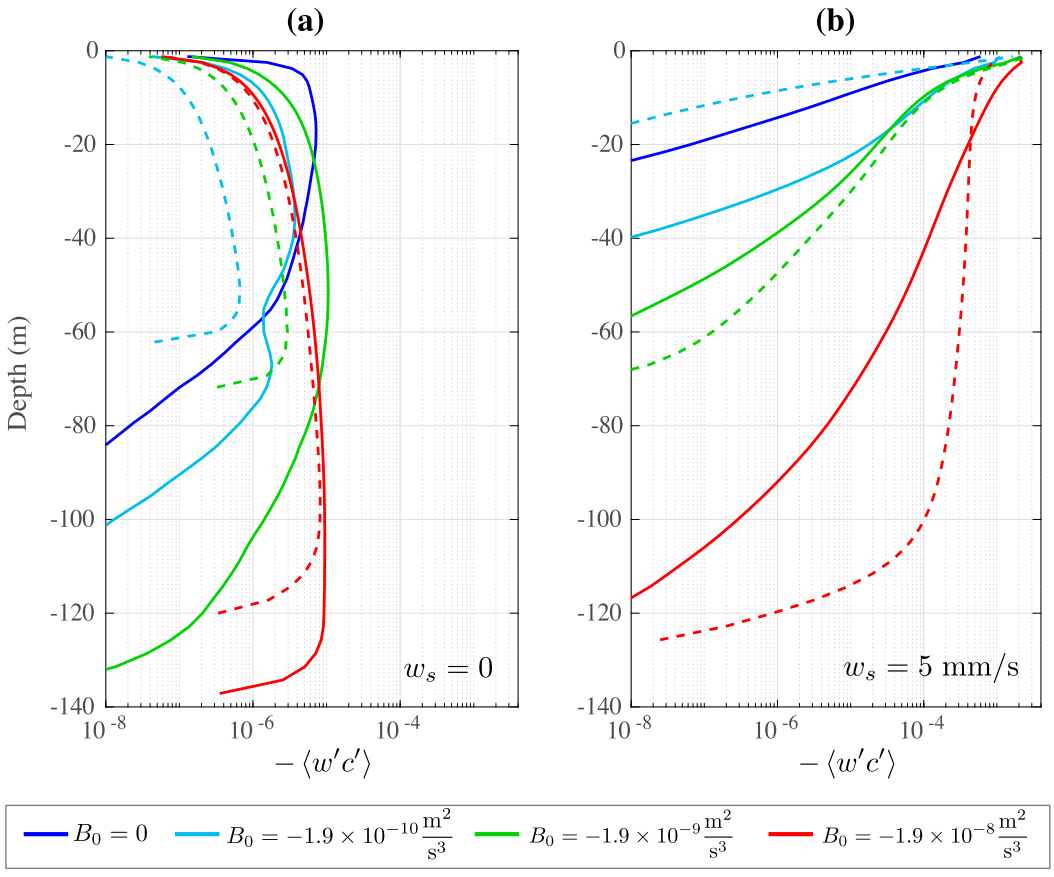

FIG. 3. Vertical profiles of the mean turbulent tracer flux $-\langle w'c' \rangle$ for (a) neutral and (b) buoyant tracers. Solid lines indicate simulations with a background horizontal density gradient of $M^2 = 3 \times 10^{-8}\,s^{-2}$, and dashed lines indicate simulations with $M^2 = 0$.

this choice ensures that submesoscales have developed before the start of the time average. The start and end of the time averaging window are marked using dots in Fig. 1a.

Relative to homogeneous turbulent convection, submesoscale activity enhances the vertical velocity for weak convective forcing while suppressing the vertical velocity for stronger forcing. This is shown in Fig. 1b, which shows vertical profiles of the root-mean-square (rms) vertical velocity for the four simulations listed in Table 1. Here, the rms is calculated with respect to an average in both horizontal directions, and the result is then averaged over the time intervals shown in Fig. 1a. Dashed lines show simulations with the same forcing strength, but without a background density front, and therefore without submesoscale activity. For all forcing strengths, the rms vertical velocity is enhanced below the mixed layer in the simulations when a background density gradient is present.

Horizontal cross sections of the vertical velocity at a depth of 25 m illustrate the onset of convection and the development of a submesoscale eddy (Fig. 2) for $B_0 = -1.9 \times 10^{-9}\,m^2\,s^{-3}$. Similar features are also seen in the other forced simulations with $M^2 \neq 0$. Early times are characterized by a relatively uniform field of convective cells (Fig. 2a), which then organize into inclined bands (Fig. 2b). After about 2 days, the convective bands have merged to form larger features and begin to show cyclonic roll-up in "comma"-like features (Fig. 2c). Finally, after about 3 days, these features merge into a single cyclonic submesoscale eddy (Fig. 2d). Once it develops, the submesoscale eddy and front persist for the rest of the simulation. Intense subduction occurs along the submesoscale front where small-scale turbulence is intensified, while other parts of the domain are relatively quiescent.

b. *Buoyant tracers*

Figure 3 shows profiles of the mean turbulent tracer flux $-\langle w'c' \rangle$ for a neutral and a buoyant tracer. Here $\langle \cdot \rangle$ denotes an average in x, y and over the time windows indicated in Fig. 1a, and primes denote departures from the horizontal average. Solid lines indicate simulations with $M^2 = 3 \times 10^{-8}\,s^{-2}$ and active submesoscales,

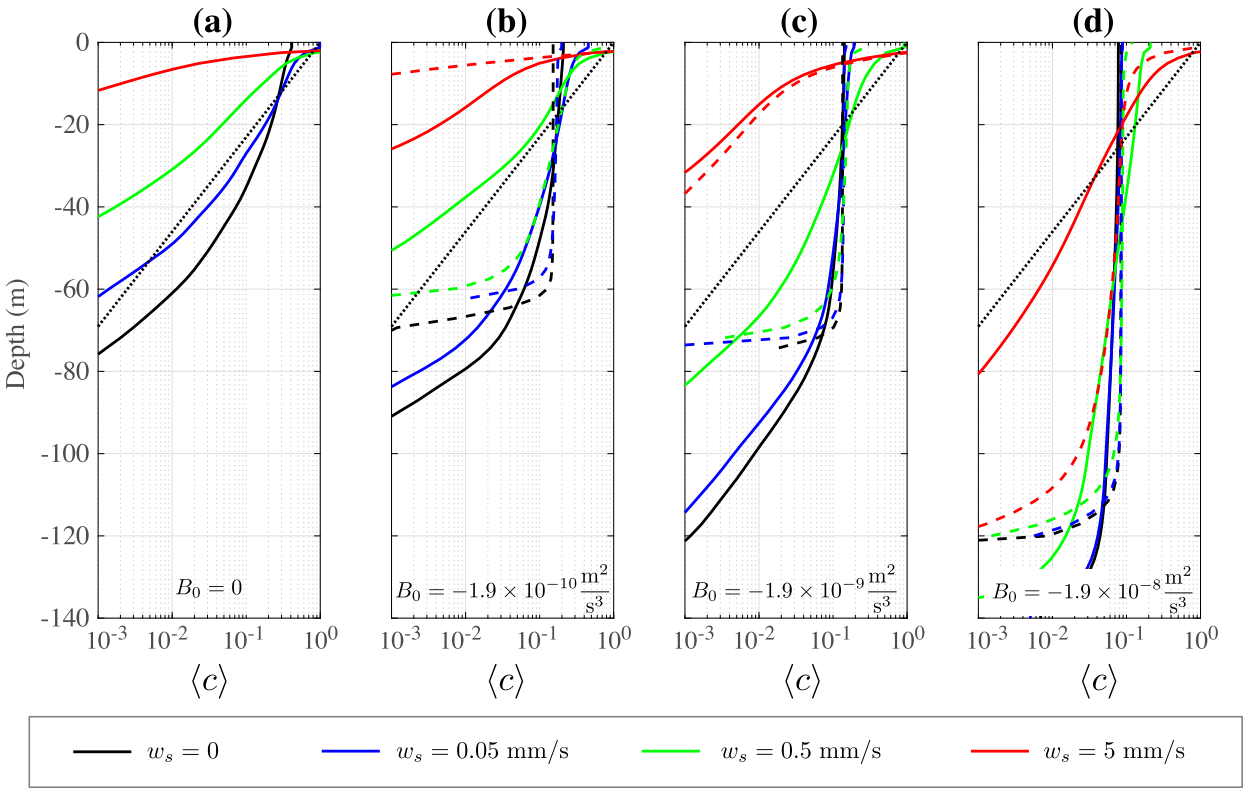

FIG. 4. Vertical profiles of the mean tracer concentrations. Solid lines indicate simulations with a background horizontal density gradient of $M^2 = 3 \times 10^{-8}\,\mathrm{s^{-2}}$, dashed lines indicate simulations with $M^2 = 0$, and dotted lines show the initial tracer concentration.

while dashed lines indicate simulations with $M^2 = 0$ and no submesoscale activity. For weak and moderate forcing, the magnitude of the tracer flux of neutral tracers (Fig. 3a) is significantly enhanced by the presence of submesoscales. However, for strong forcing ($B_0 = -1.9 \times 10^{-8}\,\mathrm{m^2\,s^{-3}}$), the neutral tracer flux is very similar with and without submesoscales. This is consistent with Taylor (2016), where submesoscales did not significantly alter the turbulent diffusivity associated with phytoplankton for strong forcing.

The mean vertical fluxes for buoyant tracers with $w_s = 5\,\mathrm{mm\,s^{-1}}$ (Fig. 3b) are qualitatively and quantitatively different compared to the fluxes of neutral tracers. For buoyant tracers with $w_s = 5\,\mathrm{mm\,s^{-1}}$, the mean vertical flux associated with buoyant rise is nearly balanced by downward mixing by turbulence; that is, $w_s\langle c \rangle \simeq -\langle w'c' \rangle$. For all forcing strengths, the magnitude of the buoyant tracer flux is maximum near the surface, reaching values 100 times larger than the maximum values for neutral tracers.

Unlike the case for neutral tracers, submesoscales have a strong influence on the vertical flux of buoyant tracers under strong forcing (cf. the solid and dashed red curves in Fig. 3b). Specifically the vertical tracer flux is more depth dependent for $M^2 = 3 \times 10^{-8}\,\mathrm{s^{-2}}$ compared with $M^2 = 0$ in the strongly forced simulation with $B_0 = -1.9 \times 10^{-8}\,\mathrm{m^2\,s^{-3}}$. The strong depth dependence of the turbulent flux of buoyant tracers is reflected in a strong depth dependence in the mean tracer concentration (see Fig. 4).

In all cases the mean concentration of buoyant tracers is surface intensified, while all tracers are advected to deeper depths in simulations with stronger forcing (see Fig. 4). In most cases the mean tracer concentration is more uniform in the mixed layer for simulations with $M^2 = 0$ (dashed lines) compared to those with $M^2 \neq 0$. This is consistent with the finding from Taylor (2016) that submesoscales suppress turbulent mixing. In all of the forced simulations, neutral and weakly buoyant tracers ($w_s = 0$ and $0.05\,\mathrm{mm\,s^{-1}}$) are advected deeper in the simulations with submesoscales present. In the simulation with $B_0 = -1.9 \times 10^{-9}\,\mathrm{m^2\,s^{-3}}$, this difference is significant. For example, in the simulation with $M^2 = 3 \times 10^{-8}\,\mathrm{s^{-2}}$, the depth where $\langle c \rangle = 0.01$ in the case with $w_s = 0$ is more than 20 m deeper than in the simulation with $M^2 = 0$ (Fig. 4c).

Although all tracers are advected by the same velocity field, the effective vertical diffusivity is larger for

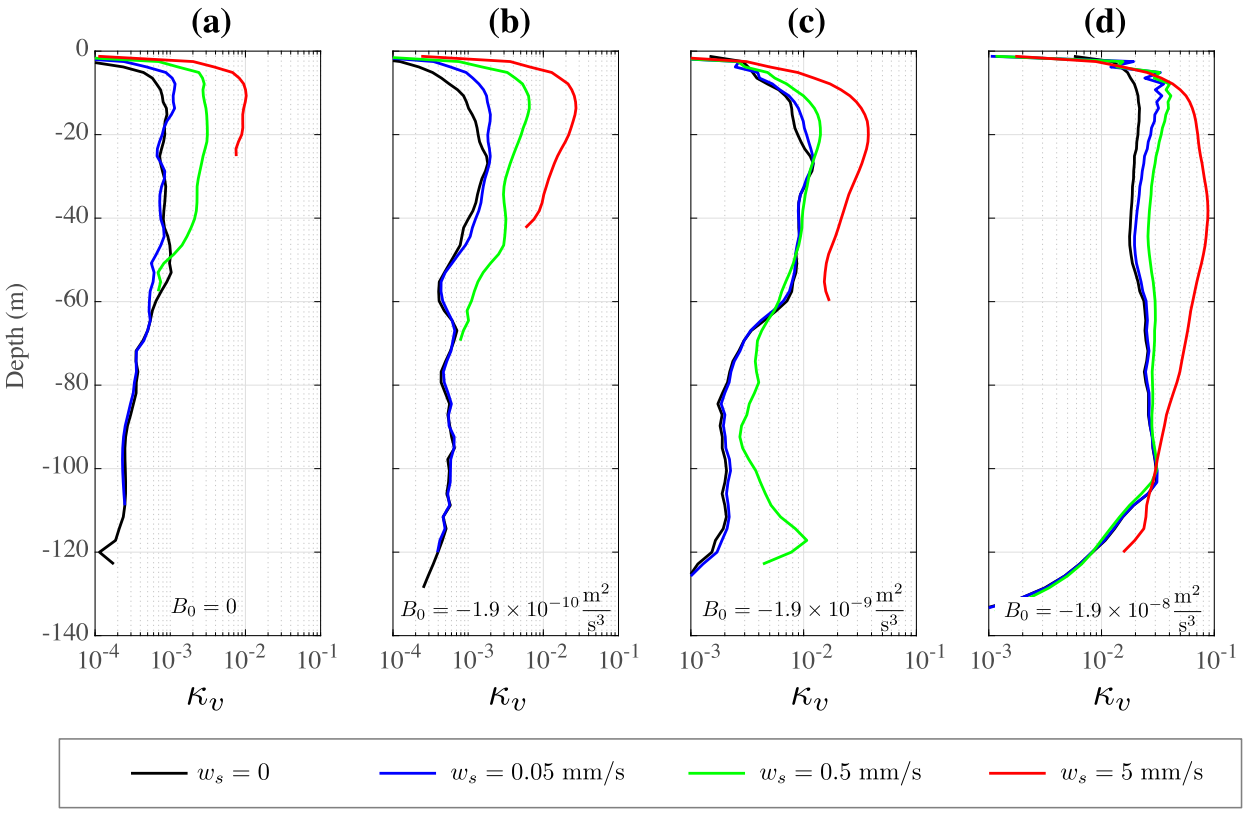

FIG. 5. (a)–(d) Effective vertical diffusivity, $\kappa_v \equiv -\langle w'c' \rangle / (\partial \langle c \rangle / \partial z)$, where angle brackets denote an average in both horizontal directions and over the time intervals indicated in Fig. 1a for different values of B_0. To avoid numerical truncation errors, only depths where $\langle c \rangle > 10^{-6}$ are shown. Note that the limits of the κ_v axis are different for (a),(b) and (c),(d).

buoyant tracers. The effective vertical diffusivity can be diagnosed by taking the ratio of the diagnosed tracer flux from the LES model and dividing by the mean tracer gradient:

$$\kappa_v(z,t,c) = \frac{-\langle w'c' \rangle}{\partial \langle c \rangle / \partial z}. \tag{5}$$

Figure 5 shows κ_v for the simulations with $M^2 = 3 \times 10^{-8}\,\mathrm{s}^{-2}$. In all cases, the diagnosed diffusivity for the tracer with the smallest slip velocity is very close to that for a neutral tracer (with $w_s = 0$). However, κ_v diagnosed for the tracer with the largest slip velocity can be more than a factor of 10 larger than κ_v for the neutral tracer. This effect becomes less pronounced for simulations with stronger forcing, but enhancement of κ_v still occurs.

It is worth emphasizing that the κ_v profiles in Fig. 5 are diagnosed for the same velocity fields. Smith et al. (2016) found that neutrally buoyant passive tracers with different initial conditions experienced different levels of κ_v in the same flow field. The cause of the difference in κ_v seen here is apparent from the spatial distributions of each tracer. Figure 6 shows horizontal slices of the tracers for the simulation with $B_0 = -1.9 \times 10^{-8}\,\mathrm{m^2\,s^{-3}}$ at the same time and depth as shown in Fig. 2d. At this depth ($z = -25\,\mathrm{m}$) the neutral and weakly buoyant tracers (Figs. 2a and 2b, respectively) are relatively well mixed. In contrast, the concentration of the more buoyant tracers is elevated near the submesoscale front where strong downwelling occurs. Nonzero concentrations of the most buoyant tracer only occur in locations coincident with strong downwelling. The correlation between high tracer concentration and negative vertical velocity enhances κ_v for buoyant tracers.

4. Conclusions and discussion

Here, large-eddy simulations (LES) have been used to study the influence of submesoscale dynamics on buoyant tracers in the upper ocean. Small-scale turbulence is generated by imposing a constant, destabilizing surface buoyancy flux, while submesoscales are generated through mixed layer instability (MLI) associated with an imposed background horizontal buoyancy gradient. A submesoscale front develops around the edge

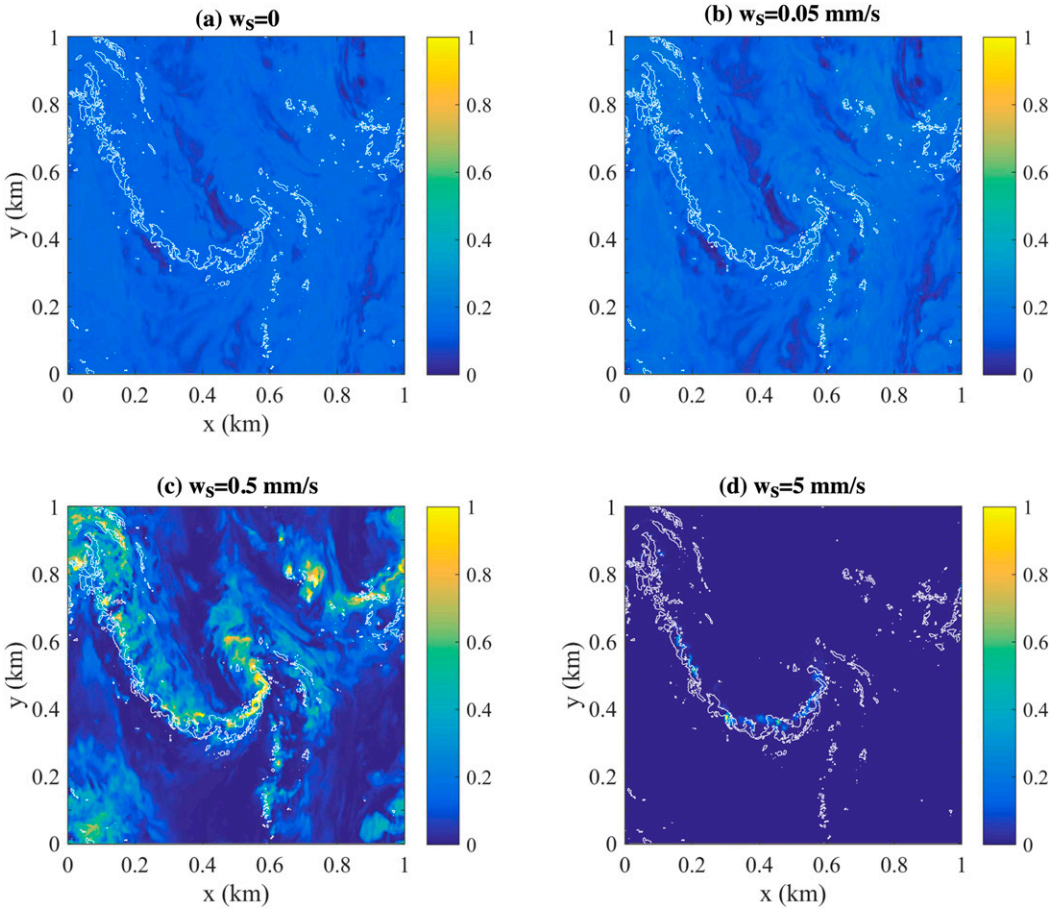

FIG. 6. Horizontal slices of various passive tracer concentrations at $z = -25$ m and $t = 3.3$ days in the simulation shown in Fig. 2 (cf. with Fig. 2d). White contours indicate regions of strong downwelling with $w = -0.005\,\mathrm{m\,s^{-1}}$.

of the submesoscale eddy, and the front is associated with enhanced small-scale turbulence and intense downwelling.

Buoyant tracers accumulate near the surface along submesoscale fronts driven by convergent horizontal flows. Strong downwelling along the submesoscale front subducts buoyant tracers and enhances the vertical diffusivity relative to a neutrally buoyant tracer. For weakly buoyant tracers and/or strong convection, the tracers remain relatively homogeneous in the mixed layer, and the strong correlation between submesoscale currents and tracer concentration is broken.

Callies and Ferrari (2018) found that submesoscale motions persist even in the presence of strong buoyant convection. In the simulations here, the vertical turbulent flux associated with neutral tracers under strong convective forcing is very similar with and without submesoscales, a result consistent with Taylor (2016). However, the same is not true for strongly buoyant tracers. In this case, submesoscale motions remain effective in accumulating buoyant tracers in regions of intense downwelling. As a result, the turbulent flux of highly buoyant tracers in strong forcing is significantly altered by the presence of submesoscales. This implies that persistent submesoscale currents seen by Callies and Ferrari (2018) under strong convective forcing have a strong influence on the transport of buoyant tracers.

These results present several challenges for ocean models. First, the submesoscale front where buoyant tracers accumulate is less than 100 m wide (see Fig. 6). Resolving fronts and filaments on this scale is challenging, even for high-resolution regional ocean models. Adding to this challenge is the observation that buoyant tracers sample the flow field differently depending on their buoyancy. Buoyant material such as oil droplets, bubbles, and microplastics are composed of a range of particle sizes and slip velocities. Particles in different size classes would then respond differently to the same flow field. This could lead to particle segregation, further

complicating efforts to model the response of buoyant material.

While these challenges might seem daunting, there are still opportunities for progress. One approach would be a statistical representation of submesoscale fronts and filaments. For example, it might be possible to use idealized models to describe the properties (e.g., width, depth, strength, frequency of occurrence) of submesoscale fronts as a function of mesoscale properties, including mixed layer depth, strain, and density gradients. Instead of resolving individual submesoscale fronts and filaments, one could represent important quantities such as the vertical flux of buoyant tracers by averaging across an ensemble of characteristic submesoscale fronts and filaments and more quiescent regions. Idealized simulations like those described here could help describe how to weight the average depending on the buoyancy of the tracers involved.

Acknowledgments. Requested Data Attribution Statement: Data are publicly available through the Gulf of Mexico Research Initiative Information & Data Cooperative (GRIIDC) at https://data.gulfresearchinitiative.org (DOI: 10.7266/N7T1520X). This work benefited from a grant from the Gulf of Mexico Research Initiative. The author is grateful for helpful comments from the CARTHE project team and three anonymous referees. Kat Smith provided helpful comments and suggestions on a draft of this paper. Supporting data can be obtained online (https://doi.org/10.17863/CAM.23250).

REFERENCES

Bachman, S. D., and J. R. Taylor, 2016: Numerical simulations of the equilibrium between eddy-induced restratification and vertical mixing. *J. Phys. Oceanogr.*, **46**, 919–935, https://doi.org/10.1175/JPO-D-15-0110.1.

Brunner, K., T. Kukulka, G. Proskurowski, and K. Law, 2015: Passive buoyant tracers in the ocean surface boundary layer: 2. Observations and simulations of microplastic marine debris. *J. Geophys. Res. Oceans*, **120**, 7559–7573, https://doi.org/10.1002/2015JC010840.

Callies, J., and R. Ferrari, 2018: Baroclinic instability in the presence of convection. *J. Phys. Oceanogr.*, **48**, 45–60, https://doi.org/10.1175/JPO-D-17-0028.1.

Capet, X., J. C. McWilliams, M. J. Molemaker, and A. Shchepetkin, 2008: Mesoscale to submesoscale transition in the California Current system. Part III: Energy balance and flux. *J. Phys. Oceanogr.*, **38**, 2256–2269, https://doi.org/10.1175/2008JPO3810.1.

Fox-Kemper, B., R. Ferrari, and R. Hallberg, 2008: Parameterization of mixed layer eddies. Part I: Theory and diagnosis. *J. Phys. Oceanogr.*, **38**, 1145–1165, https://doi.org/10.1175/2007JPO3792.1.

Kukulka, T., and K. Brunner, 2015: Passive buoyant tracers in the ocean surface boundary layer: 1. Influence of equilibrium wind-waves on vertical distributions. *J. Geophys. Res. Oceans*, **120**, 3837–3858, https://doi.org/10.1002/2014JC010487.

Mahadevan, A., A. Tandon, and R. Ferrari, 2010: Rapid changes in mixed layer stratification driven by submesoscale instabilities and winds. *J. Geophys. Res. Oceans*, **115**, C03017, https://doi.org/10.1029/2008JC005203.

——, E. D'Asaro, C. Lee, and M. J. Perry, 2012: Eddy-driven stratification initiates North Atlantic spring phytoplankton blooms. *Science*, **337**, 54–58, https://doi.org/10.1126/science.1218740.

Omand, M. M., E. A. D'Asaro, C. M. Lee, M. J. Perry, N. Briggs, I. Cetinić, and A. Mahadevan, 2015: Eddy-driven subduction exports particulate organic carbon from the spring bloom. *Science*, **348**, 222–225, https://doi.org/10.1126/science.1260062.

Shakespeare, C. J., and J. Taylor, 2014: The spontaneous generation of inertia–gravity waves during frontogenesis forced by large strain: Theory. *J. Fluid Mech.*, **757**, 817–853, https://doi.org/10.1017/jfm.2014.514.

——, and ——, 2015: The spontaneous generation of inertia–gravity waves during frontogenesis forced by large strain: Numerical solutions. *J. Fluid Mech.*, **772**, 508–534, https://doi.org/10.1017/jfm.2015.197.

——, and ——, 2016: Spontaneous wave generation at strongly strained density fronts. *J. Phys. Oceanogr.*, **46**, 2063–2081, https://doi.org/10.1175/JPO-D-15-0043.1.

Smith, K. M., P. E. Hamlington, and B. Fox-Kemper, 2016: Effects of submesoscale turbulence on ocean tracers. *J. Geophys. Res. Oceans*, **121**, 908–933, https://doi.org/10.1002/2015JC011089.

Stone, P. H., 1966: On non-geostrophic baroclinic stability. *J. Atmos. Sci.*, **23**, 390–400, https://doi.org/10.1175/1520-0469(1966)023<0390:ONGBS>2.0.CO;2.

Taylor, J. R., 2008: Numerical simulations of the stratified oceanic bottom boundary layer. Ph.D. thesis, University of California, San Diego, 212 pp.

——, 2016: Turbulent mixing, restratification, and phytoplankton growth at a submesoscale eddy. *Geophys. Res. Lett.*, **43**, 5784–5792, https://doi.org/10.1002/2016GL069106.

——, and R. Ferrari, 2010: Buoyancy and wind-driven convection at mixed layer density fronts. *J. Phys. Oceanogr.*, **40**, 1222–1242, https://doi.org/10.1175/2010JPO4365.1.

——, and ——, 2011: Ocean fronts trigger high latitude phytoplankton blooms. *Geophys. Res. Lett.*, **38**, L23601, https://doi.org/10.1029/2011GL049312.

Thomas, L. N., 2005: Destruction of potential vorticity by winds. *J. Phys. Oceanogr.*, **35**, 2457–2466, https://doi.org/10.1175/JPO2830.1.

——, A. Tandon, and A. Mahadevan, 2008: Submesoscale processes and dynamics. *Ocean Modeling in an Eddying Regime*, *Geophys. Monogr.*, Vol. 177, Amer. Geophys. Union, 17–38.

Thorpe, S., 2000: Langmuir circulation and the dispersion of oil spills in shallow seas. *Spill Sci. Technol. Bull.*, **6**, 213–223, https://doi.org/10.1016/S1353-2561(01)00040-8.

Veron, F., and W. K. Melville, 2001: Experiments on the stability and transition of wind-driven water surfaces. *J. Fluid Mech.*, **446**, 25–65.